Density functional description of spin, lattice, and spin-lattice dynamics in antiferromagnetic and paramagnetic phases at finite temperatures

Davide Gambino [1], Oleksandr I. Malyi [2,*], Zhi Wang [2,3], Björn Alling [1], and Alex Zunger [2,†]

[1] *Department of Physics, Chemistry and Biology (IFM), Linköping University, SE-58183 Linköping, Sweden*

[2] *Renewable and Sustainable Energy Institute, University of Colorado, Boulder, Colorado 80309, USA*

[3] *State Key Laboratory for Superlattices and Microstructures, Institute of Semiconductors, Chinese Academy of Sciences, Beijing 100083, China*

(Received 1 March 2022; revised 21 August 2022; accepted 22 August 2022; published 10 October 2022)

Describing the (a) electronic and magnetic properties (EMPs) of compounds generally requires the specification of (b) the type of spin configurations one is considering [e.g., antiferromagnetic (AFM) or paramagnetic (PM) phases, with or without spin short-range order (SRO)] and lattice structure (e.g., atomic displacements, possible symmetry breaking) of such phases at a given temperature. Indeed, studying the interplay between the spin configuration and lattice structure (SCLS) and the ensuing EMPs has been an outstanding challenge in the theory of matter. The traditional approach of electronic phases of matter has generally focused on the interelectronic interactions, regarding the lattice structure as a spectator degree of freedom (DOF), often fixed from an external source (experiment or model assumptions). However, one expects that the EMPs of a compound can generally respond self-consistently to changes in SCLS (including symmetry), and at the same time, the SCLS can change in response to different electron and spin distributions visited during the calculation of the EMPs. This ping-pong-like interplay where structure affects electronic properties and the latter affect structure is indeed a cornerstone of much of the intricacy of understanding quantum materials. However, there is a limited understanding of the theory required to determine the SCLS at finite temperature in a way that can affect the EMPs and vice versa. We use here a practical, density functional theory (DFT)-based approach that provides the SCLS as a function of temperature, involving the description of spin, lattice, and spin-lattice dynamics of AFM and PM phases, thus providing the required ping-pong partners to the description of the EMPs of different phases. We distinguish three levels of dynamics: (I) dynamics of the spin DOFs treated via noncollinear Heisenberg Monte Carlo solved with exchange energies obtained from first-principles DFT cluster expansion, (II) dynamics of the lattice DOFs treated by *ab initio* molecular dynamics (AIMD) employing a fixed, representative spin configuration from Level I at the simulated temperature, and (III) coupling of spin and lattice dynamics via Landau-Lifshitz-Gilbert spin dynamics combined with AIMD. Such SCLSs at each of the three levels are used as inputs to DFT supercell calculations, providing the EMPs at each temperature. The results of this sequence include electronic band structures, bandgaps, density of states, as well as the statistical distribution of local moments and the SRO parameters, each as a function of temperature. Herein, we define a path to include temperature in magnetic insulators at different levels of spin dynamics by intercommunication between electronic structure theory and statistical mechanics. Using NiO as a test case, we address the separability of the DOFs in magnetic insulators for a minimal description of EMPs, demonstrating that inclusion of spin dynamics and, to some level, lattice dynamics is enough to explain the EMPs.

DOI: 10.1103/PhysRevB.106.134406

I. INTRODUCTION

In dealing with electronic and magnetic structure of matter, one faces contributions from the electronic system as well as contributions from lattice structure, including local degrees of freedom (DOFs). Such theories of electronic and magnetic properties (EMPs) at finite temperatures require the knowledge of the spin configuration and lattice structure (SCLS). Description of the EMPs includes selecting a level of theory needed for describing the fundamental electron-electron interactions (such as mean-field or many-body approaches), whereas the SCLS requires the knowledge of spin configurations one is considering [e.g., antiferromagnetic (AFM) or paramagnetic (PM) phases, with or without spin short-range order (SRO)] and lattice structure (including atomic displacements, possible symmetry breaking involved) of such phases at a given temperature, in a semiclassical picture of magnetic materials.

The separation of the EMPs from the spin and lattice configurations has been an outstanding problem in this field.

*Present address: ENSEMBLE3 Centre of Excellence, Wolczynska 133, 01-919 Warsaw, Poland.

†alex.zunger@colorado.edu

The extreme approach of the theory of electron phases (as in the Mott-Hubbard problem, exotic phases, and quantum spin liquids) deals primarily with the electron part of the problem while regarding the lattice motifs as largely a nonresponsive, spectator DOF. However, it has been recognized that EMPs of a phase generally respond self-consistently to changes in the SCLS and vice versa, in a *ping-pong-like fashion*: structural relaxation, positional or magnetic symmetry breaking, or different spin configurations (all being DOFs of the SCLS) can drastically affect the ensuing predicted EMPs and vice versa. At the same time, the choices of the type of interelectronic interaction used in predicting the EMPs can affect the predicted ensuing SCLS.

The complexity of developing appropriate computational methods that deal with electron/spin DOFs along with structure has historically steered solid-state physics to arguing (frequently postulating) a decoupling between the microscopic DOFs (m-DOFs) underlying the EMPs from those underlying the SCLS as its historical standard modus operandi. Disappointingly, not all attempts to separate the dynamics of different m-DOFs into nonoverlapping domains were as successful as the Frank-Condon adiabatic separation. For instance, in magnetism, the often-asserted finite but weak coupling [1–5] between the ionic vibration timescale and spin dynamics timescales has become an accepted truth. Examples include the conventional three-temperature model (3TM) [1], which uses three individual sets of temperatures and heat capacities from the spin moment, electron, and lattice, with phenomenological factors to describe the coupling among different sets (often extracted from the signal fitting process from experimental measurement). The simplified 3TM approach as well as the absence of an atomistic description of the m-DOFs has motivated other, more advanced models, including the Elliott-Yafet scattering model [6,7], where spin flips absorb/excite phonons with a given probability, or the atomistic spin dynamics (ASD) approach based on the Landau-Lifshitz-Gilbert (LLG) equation [8,9], and the microscopic 3TM method [5]. A difficulty in such model Hamiltonian methods is that there exist empirical or phenomenological factors that are not derived by the theory itself but sometimes introduced *ad hoc* to explain observations. In this situation, it appears important to critically test these assumptions of decoupled DOFs beyond the static approximation.

A method that tries to tackle the problem of coupling between magnetic and phonon DOFs is the spin-lattice dynamics [10,11], where a Hamiltonian composed of magnetic and lattice parts is employed, and the spin and lattice m-DOFs are evolved with LLG and Newton's equations, respectively. The parameters of the Hamiltonian can be calculated *ab initio*; however, this method inherits all the problems of interatomic potentials concerning accuracy and transferability. The effect of a completely disordered picture of the PM state on vibrations and electronic structure has also been investigated [12], neglecting the temperature dependence for the spin m-DOFs. Recently, a step toward the complete simulation from first principles of magnetic materials with all electronic, magnetic, and lattice m-DOFs has been made with the introduction of LLG spin dynamics coupled with *ab initio* molecular dynamics (AIMD) [13], or the ASD-AIMD method, where electrons are treated explicitly, and interatomic forces are calculated on the density functional theory (DFT) quantum mechanical self-consistent level. This method, in contrast to spin-lattice dynamics methods based on interatomic potentials [10,11], enables a direct investigation of electronic properties: ASD-AIMD was employed in Ref. [13] to investigate the effect of magnetic DOFs at finite temperatures in the PM state on phonon properties in CrN, a narrow gap semiconductor. The result of that study was that, although the magnetic DOF in the PM state has a short time scale (on account of CrN being narrow gap), the adiabatic separation of magnetic and vibrational DOFs is not really justified. It is therefore important to assess the validity of such separations in different material systems and properties. Particularly, (i) an assessment of the effect of the coupled spin-lattice dynamics on the electronic band structure as compared with models which consider separately spin or lattice DOFs is still lacking. Likewise, (ii) a framework enabling the comparison of models with disjoint DOFs against a coupled model will be desirable. In addition, (iii) the coupling will have different effects in systems ranging from insulators to metals, therefore requiring a framework which can accommodate the whole spectrum of possible electronic properties of materials systems. The computational platform offered in this paper (Fig. 1) is designed to address these three issues.

Building on the knowledge obtained from Ref. [13], in this paper, we investigate the interrelation between electronic structure and magnetic and vibrational DOFs by using a method that combines on-the-fly statistical mechanics of finding spin configurations and the lattice structure (the SCLS) with electronic structure (the EMP). This allows one to examine how the treatment of the electronic DOFs affects the structural DOFs and how the structure in turn affects the EMPs. To examine the concept of separability of distinct DOFs, we deliberately separate different levels of dynamics of spin and lattice. Specifically, we will examine the validity of separating lattice DOFs and spin dynamics by calculating these events first congruently and then separately within dynamic DFT. This will test the common assumption that these three dynamics are well decoupled from each other, thus advancing our understanding in joint simulations of lattice and spin dynamics. Finally, the electronic Hamiltonian is deliberately selected as mean field like DFT (albeit temperature dependent), rather than leapfrogging to strongly correlated methodologies. However, the description of EMPs is executed within a larger-than-minimal unit cell of the appropriate global symmetry so that positional or spin symmetry-breaking events (reflected in the SCLS) are allowed to occur if they lower the total energy. This approach allows us to examine if the error of traditional mean-field band theory, predicting incorrectly a metallic state in 3*d* Mott oxides, reflects the absence of strong correlation (in the EMP) or the use of inappropriate SCLS that had limited symmetry breaking [14–16].

Table I summarizes the three levels of dynamics that will be described in this paper. Level I consists of only spin dynamics in a frozen lattice (avoiding phonon effect). It was done by generating many spin configurations via the noncollinear Heisenberg Monte Carlo (MC) method and using them with a frozen lattice as inputs to DFT calculations to obtain magnetic and electronic properties. Level II is the AIMD (following the *ab initio* forces from DFT) with a

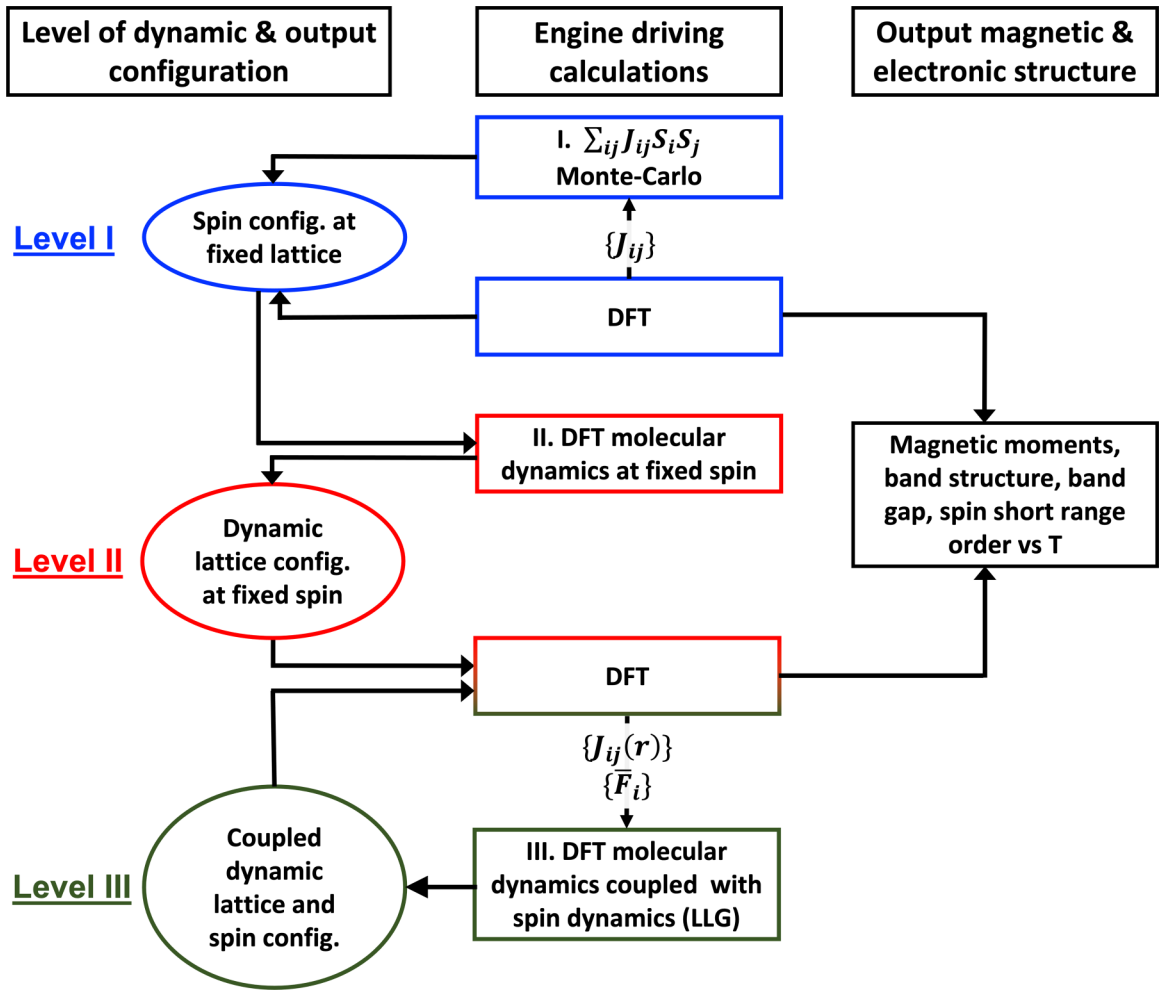

FIG. 1. Workflow of the three levels of dynamics. In Level I, we calculated with density functional theory (DFT) the exchange interactions on the static lattice, which are then used in Monte Carlo simulations with the noncollinear Heisenberg Hamiltonian to generate several spin configurations. These configurations are the input for the DFT calculations on the static lattice, which give as output the magnetic and electronic structure properties at each temperature. In Level II, we employ one single frozen spin configuration from Level I at each temperature to carry out *ab initio* molecular dynamics (AIMD) simulations at the corresponding temperature. Several spin-lattice snapshots from the simulations are taken to perform additional DFT calculations to obtain the output magnetic and electronic structure properties at each temperature. In Level III, we calculated the pair distance-dependent exchange interactions to have the coupling between the lattice and spin microscopic degrees of freedom (m-DOFs). With these interactions parametrized, we carried out coupled spin and molecular dynamics simulations with *ab initio* forces at each considered temperature, where both the spin and lattice m-DOFs are evolved simultaneously. Joint spin-lattice snapshots are then taken to perform further DFT calculations and obtain the output magnetic and electronic structure properties at each temperature.

representative frozen spin configuration taken from Level I. Level III is our joint description, based on the LLG spin dynamics with interactions and feedbacks from a vibrating lattice from DFT calculations. In Levels I and II, the effect of thermal expansion and lattice vibrations on the pair exchange interactions is neglected, whereas for Level III, the pair exchange interactions are dependent on the pair distance. This dependence, together with the spin dependence of the interatomic forces, provides the coupling between spin and lattice m-DOFs.

Each of the three levels gives coupled spin and structural configurations, which are used as inputs to the DFT

TABLE I. Summary of three levels of spin-lattice dynamics theory used in this paper.

Level of dynamics	Dynamic DOF	Frozen DOF	Simulation method for SCLS	Calculation method for EMPs
Level I	Spin	Lattice	Heisenberg MC (exchange energies from DFT)	Mean-field DFT
Level II	Lattice	Spin	AIMD	
Level III	Spin + lattice	–	LLG dynamics with AIMD	

self-consistent Hamiltonian solver to obtain the magnetic and electronic consequences of the whole dynamics, including single-particle electronic properties such as density of states (DOS), bandgaps, the unfolded E vs k dispersion (band structure), as well as magnetic properties such as local magnetic moments, local motifs, and SROs. All details of these three levels of theory are given in Sec. II. In this paper, we choose one of the most famous and classical Mott insulators NiO as the example of our joint description to study the properties under different temperatures (300–700 K) across the Néel transition $T_N = 523$ K [17]. The choice of NiO is furthermore motivated from available experimental works [18–21] that suggested existence of spin-lattice coupling effects in this compound and by an analysis of the magnetic and vibrational timescales shown in Appendix A. We find that, while the consideration of uncoupled magnetic and lattice dynamics is important for a quantitative understanding of the electronic properties and temperature evolution of the bandgap in NiO, this system does not represent a case where the dynamical coupling of these m-DOFs has a crucial impact on the EMP. In this paper, we establish a framework for estimating which phases of matter come out with weak, medium, or strong coupling of electronic, magnetic, and vibrational m-DOFs, without assumptions on the nature of the material system at hand. The current test case is the insulator NiO, but the present methodology is readily applicable to small-bandgap semiconductors and metals as well, defining a path to investigate the unknown trends of spin dynamics as an insulator becomes a metal.

II. THREE LEVELS OF DYNAMICS

Figure 1 shows the workflow of the present investigation, describing the three levels of dynamics, coupled with the corresponding electronic structure calculations; the different levels of dynamics are presented in this section. The general workflow consists of the generation of spin-lattice configurations at different temperatures, which are the input for DFT calculations, from which the temperature-dependent properties are then obtained. The calculated EMPs are magnetic moments, band structure, bandgap, and spin SRO.

A. Level I dynamics: Spin dynamics in a frozen lattice via noncollinear Heisenberg MC using DFT-determined exchange energies

As shown in Fig. 1, for all levels of dynamics, we employ the Heisenberg Hamiltonian (noncollinear magnetization) [22] to describe the spin-spin interaction and then derive the spin configurations. The Heisenberg Hamiltonian is defined only by the directions of the moments $\hat{\boldsymbol{\mu}}_i$ and spin-exchange interactions J_{ij}:

$$H = -\sum_{i \neq j} J_{ij} \hat{\boldsymbol{\mu}}_i \cdot \hat{\boldsymbol{\mu}}_j. \tag{1}$$

This is the basic formulation of the Hamiltonian, but extensions to include further effects such as distance dependence of the exchange interactions [13,23], longitudinal spin fluctuations [24–26], and higher-order terms [27,28] have been developed. The Heisenberg Hamiltonian can model spin waves [4] in materials, although it has issues mainly concerning the low-temperature behavior of magnetic materials in general (e.g., low-temperature specific heat), and antiferromagnets in particular [29]. Nonetheless, the generalized Heisenberg Hamiltonian enables a microscopic description of the main features of the magnetic m-DOF.

The Heisenberg MC simulations at all temperatures are carried out with exchange interactions calculated at the equilibrium, 0 K lattice parameter. The exchange interactions of Eq. (1) have been calculated with the cluster expansion structure inversion method [30] employing 10 ordered magnetic structures. The energy of these 10 structures with different spin configurations is calculated with DFT, followed by a cluster expansion in terms of spin interactions up to second and eighth interaction shells. The exchange interactions J_{ij} are then retrieved by matrix inversion. The Néel transition temperature (T_N) is obtained by inspection of the specific heat as a function of temperature, where the temperature with highest specific heat is taken as the T_N (see details on Level I dynamics and calculations of Heisenberg exchange interactions in Appendix B). Inclusion of eight interaction shells does not improve the estimated T_N as compared with two interaction shells (see Appendix B). We therefore consider at all levels magnetic interactions only up to next-nearest neighbors in the metal sublattice. Since in this level we employ MC simulations, the dynamics of the spins is not real-time dynamics but rather the evolution of spin configurations without a specific timescale.

From this level, we obtained a set of coupled spin-lattice configurations at each temperature, where the lattice structure is the rock salt cubic structure with ions on ideal lattice positions. In all levels, we employ a supercell made of two repetitions in the x, y, and z directions of the conventional rock salt cell.

B. Level II dynamics: *Ab initio* lattice (molecular) dynamics with a frozen spin configuration taken from Level I

In Level II, as shown in Fig. 1, we choose one single representative frozen spin orientation from Level I for each temperature T and now allow all internal atomic positions to evolve by AIMD. The spin configuration on all sites is kept frozen during AIMD with the use of constrained DFT. For each temperature, the AIMD simulation is carried out with the corresponding experimental lattice parameters from Ref. [31]. Since the spin configurations are taken from Level I, in this level, there is no effect of thermal expansion or lattice vibrations on the exchange interactions and, therefore, on the spin configuration. Of course, as the spin configurations are all taken from Level I, the first two levels of dynamics share the same exchange interactions. Appendix C provides details on the AIMD.

C. Level III dynamics: Coupled spin and lattice dynamics

As shown in Fig. 1, Level III includes the coupled spin and lattice dynamics. To account for the coupling of spin and lattice dynamics, we performed ASD-AIMD [13] simulations by using distance-dependent exchange interactions $J_{ij}(r_{ij})$ and

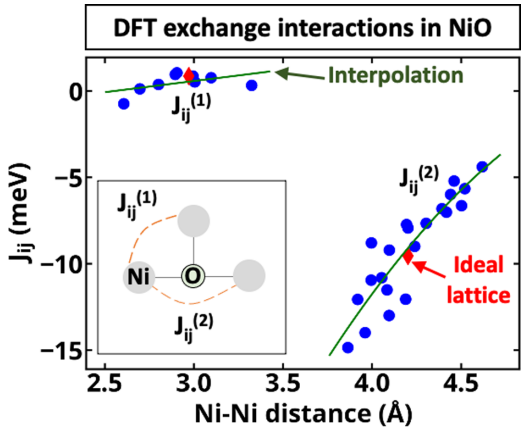

FIG. 2. Exchange interactions between first and second nearest neighbors as a function of pair distance calculated on a vibrating lattice (blue dots). The values calculated on the ideal lattice (red diamonds) are shown as a comparison. The interpolation used in the atomistic spin dynamics - *ab initio* molecular dynamics (ASD-AIMD) simulations is shown as a green line. The inset gives a schematic view of the interaction between Ni moments in the first and second interaction shell.

LLG equations:

$$\frac{\partial \hat{\boldsymbol{\mu}}_i}{\partial t} = -\frac{\gamma}{1+\alpha^2}\hat{\boldsymbol{\mu}}_i \times (\mathbf{H}_{\text{eff}} + \mathbf{b}_i) - \gamma \frac{\alpha}{1+\alpha^2}\hat{\boldsymbol{\mu}}_i \times \{\hat{\boldsymbol{\mu}}_i \times (\mathbf{H}_{\text{eff}} + \mathbf{b}_i)\}, \quad (2)$$

where $\hat{\boldsymbol{\mu}}_i$ is the direction of moment $\boldsymbol{\mu}_i$, γ and α are the electron gyromagnetic ratio and the phenomenological damping factor, respectively, whereas $\mathbf{b}_i$ is the random magnetic field employed to enforce the right temperature T, as done in Langevin dynamics. Here, $\mathbf{H}_{\text{eff}}$ is the effective magnetic field experienced by moment $\boldsymbol{\mu}_i$ due to all the other moments in the solid, and it is expressed as

$$\mathbf{H}_{\text{eff}} = -\frac{1}{\mu_i}\frac{\partial H^{\text{Heisenberg}}}{\partial \hat{\boldsymbol{\mu}}_i}, \quad (3)$$

with $H^{\text{Heisenberg}}$ being the Heisenberg Hamiltonian [Eq. (1)] modified by the employment of the distance-dependent exchange interactions. Notice that the size of the local moments μ_i enters into the LLG equations only through the effective field $\mathbf{H}_{\text{eff}}$. In short, for each AIMD step that we perform, we obtain new atomic positions and atomic pair distances r_{ij}, from which we recalculate the exchange interactions $J_{ij}(r_{ij})$ according to the parametrization shown in Fig. 2. The updated exchange interactions are fed into the ASD code, which updates the direction of the moments employed in the next AIMD step. The details of the ASD-AIMD simulation protocol are described in Ref. [13]. The experimental lattice constant of NiO [31] at each temperature is employed in the simulations.

It is important to notice that the coupled dynamics can occur only through the distance-dependent $J_{ij}(r_{ij})$ since this is the only mechanism considered here which enables the influence of the lattice DOF on the magnetic DOF; the opposite influence of the magnetic DOF on the vibrations occurs through the evolving spin configurations. An additional difference between Levels I/II and III is that, in the former, there is no consideration of the effect of thermal expansion on the exchange interactions. However, thermal expansion in the range of temperatures considered here leads to changes in the exchange interactions of 0.2 meV, which do not induce any quantitatively relevant change on the results of the three different levels of dynamics. Therefore, the main difference between Levels I/II and III stems from the explicit lattice vibrations and their effect on the exchange interactions, together with the coupled spin dynamics.

The exchange interactions of Eq (1) up to shells of the second nearest neighbors as a function of pair distance were calculated as described in Ref. [23] and detailed in Appendix D. The resulting exchange interactions are shown in Fig. 2 (blue dots) for first and second nearest neighbors, respectively, together with the ideal lattice values (red diamonds) and the interpolation (green line) employed then in ASD-AIMD for Level III.

III. CALCULATING PHYSICAL PROPERTIES FROM LEVEL I–III SIMULATIONS

For every temperature T, using the coupled spin and positional configurations $\{S_i^{(\text{I})}\} - \{d_i^{(\text{I})}\}$, $\{S_i^{(\text{II})}\} - \{d_i^{(\text{II})}\}$, and $\{S_i^{(\text{III})}\} - \{d_i^{(\text{III})}\}$ calculated from Levels I–III for a number of snapshots $t(T)$, we utilize DFT to extract the physical properties using Perdew-Burke-Ernzerhof (PBE) + U calculations [32,33] with U of 5 eV applied to Ni-d states as implemented in VASP [33–37]. For each SCLS, as its spin and/or lattice dynamics have already been done in Levels I–III, it is used as the input to DFT calculations without further changes. This is done by constrained noncollinear DFT keeping the directions of the magnetic moments and the lattice structure frozen. The cutoff energy was fixed to be 500 eV for all calculations. All DFT calculations at this point are preformed using a $4 \times 4 \times 4$ Γ-centered Monkhorst-Pack grid [38].

We emphasize that the actual role of an interelectronic onsite repulsion U in the Hubbard Hamiltonian treatment (a strong correlation role) is rather different from the role of U in DFT + U formalism (where the actual role of this pseudo-U is in effect a self-interaction-like correction that renders orbitals more spatially compact and downshifts the orbital energy). Indeed, it has been shown [14,39] that a more proper exchange-correlation DFT functional can nonempirically provide certain effects previously attributed to strong correlation in DFT self-consistent calculations without U, such as gapping of Mott insulators.

A. Calculation of the local magnetic moments in AFM and PM phases

The local magnetic moments are obtained from DFT since, especially for Level I, the size of the moments from the input spin configurations has little meaning (Heisenberg Hamiltonian, Eq. (1), considers fixed size of the moments). To calculate the distribution of local magnetic moments for every site in each snapshot, we calculate the local magnetic moment as $\mu_i = \sqrt{\mu_{i,x}^2 + \mu_{i,y}^2 + \mu_{i,z}^2}$, where $\mu_{i,x}$, $\mu_{i,y}$, and $\mu_{i,z}$

are corresponding projections of noncollinear local magnetic moment on the x, y, and z axes.

B. Calculation of the local spin motifs

The local spin motifs (LSMs) for atom i at time t are defined as

$$\mathrm{LSM}(i,t) = \frac{1}{N_{\mathrm{neighbors}}} \sum_{j=1}^{N_{\mathrm{neighbors}}} \hat{\boldsymbol{\mu}}_i(t) \cdot \hat{\boldsymbol{\mu}}_j(t), \tag{4}$$

where $N_{\mathrm{neighbors}}$ is the number of neighbors of magnetic atom i in the corresponding coordination shell, and all other quantities were previously defined. We carried out analysis of the distribution of LSMs for first and second coordination shells at every temperature and level.

C. Calculation of SRO

The SRO for a particular coordination shell is calculated as

$$\mathrm{SRO(shell)} = \frac{1}{|\mu_{\mathrm{AFM}}|^2 N_{\mathrm{snapshots}}} \sum_{t=1}^{N_{\mathrm{snapshots}}} \langle \hat{\boldsymbol{\mu}}_i(t) \cdot \hat{\boldsymbol{\mu}}_j(t) \rangle_{\mathrm{shell}}, \tag{5}$$

$$\langle \hat{\boldsymbol{\mu}}_i(t) \cdot \hat{\boldsymbol{\mu}}_j(t) \rangle_{\mathrm{shell}} = \frac{1}{N_{\mathrm{atoms}}} \sum_{i=1}^{N_{\mathrm{atoms}}} \frac{1}{N_{\mathrm{neighbors}}} \sum_{j=1}^{N_{\mathrm{neighbors}}} \hat{\boldsymbol{\mu}}_i(t) \cdot \hat{\boldsymbol{\mu}}_j(t). \tag{6}$$

Here, $N_{\mathrm{snapshots}}$ is the number of snapshots employed, N_{atoms} is the number of magnetic atoms in the supercell (32 in our case), and $|\mu_{\mathrm{AFM}}|^2$ is the modulus squared of the local moments in the AFM ground state, used as the normalization value.

D. Calculation of DOS

The DOS is calculated by averaging the DOS computed for 40 different snapshots and aligned O-1s core levels:

$$\mathrm{DOS} = \frac{\sum_t^{N_{\mathrm{snapshots}}} \mathrm{DOS}(t)}{N}. \tag{7}$$

We carried out the alignment with respect to the core levels because the mean energy of O-1s states is roughly a constant for different snapshots at the same temperature. The same tendency is observed for all levels (the largest change in position of core states in snapshots is 0.06 eV at $T = 700$ K in Level III).

E. Calculation of unfolded band structures

The supercell approach applied in Levels I–III, although allowing all different types of DOFs, suffers from the very dense band structure due to the folding mechanism in the small reciprocal-space Brillouin zones of the large real-space cell sizes. With the help of rigorous band unfolding [here, the effective band structure (EBS)] method [40–42], one can restore the E-vs-k dispersive features, both coherent and incoherent, from the spectral functions of supercell band structures unfolded back into the primitive Brillouin zone. The unfolded band structure at each temperature was calculated as the superposition of the EBS for 10 snapshots. A consistency test of band structures and gap values from EBS superpositions on the number of snapshots considered has been done up to 20 snapshots for each superposition, and we have found that the superposition over 10 EBSs shows good convergence with respect to the gap values. Appendix E provides details on the superposition of unfolded band structures of the supercells.

F. Calculation of bandgap energy

The *bandgap energy*, calculated both from DOS and EBS, is defined as the energy difference between band edges having intensity larger than some critical values (i.e., 0.1 eV^{-1} atom^{-1} for DOS and the spectral functions stronger than 0.1 Å eV^{-1} atom^{-1} for EBS). We note that the bandgap energies obtained from this paper should be compared with the gaps from photoemission or angle-resolved photoemission spectroscopy but not to the gaps from absorption spectroscopy or mobility measurement, as the gap calculations in this paper consider the DOS rather than transitions from state to state or electronic mobility.

IV. RESULTS

We start the presentation of this section by summarizing the main results.

First of all, at all temperatures investigated starting from 300 K (AFM below the Néel temperature T_{N}) to 700 K (PM, above the Néel temperature), NiO is an insulator with a finite gap. In this range, NiO shows a distribution of local magnetic moments, which is not only in contrast to the ground-state AFM phase (all Ni sites have a uniform moment) but also in sharp contrast to the aforementioned nonmagnetic approach applied in naïve DFT. Different levels of theory (Levels I–III) give only small differences in the distributions of local magnetic moments. In all cases, the average local moment on Ni is 1.7 μB. This clearly demonstrates that the PM phase of NiO at finite temperature cannot be described as a nonmagnetic global average structure, which has been rather a common approximation in motivating the development of post-DFT methods [e.g., dynamical mean-field theory (DMFT)] [43,44].

In addition, temperature induces a change in the distribution of local magnetic motifs at all levels of spin-lattice dynamics. Even below the Néel temperature but above 0 K, NiO cannot be described as a perfectly long-range ordered AFM structure but indeed should be described using a large supercell with given SRO.

Temperature also induces a reduction of the bandgap of 0.2–0.6 eV from 300 to 700 K in NiO at all levels of dynamics, together with a broadening of DOS as temperature increases. The gap reduction and DOS broadening in Level I are smaller than that in Levels II and III, while the results of the latter two levels are relatively consistent with each other. It indicates that both spin and lattice dynamics have nonnegligible contributions to the gap renormalization; however, the coupling of the two dynamics has only weak effects on the gap.

Finally, for every temperature, by comparing individual unfolded band structures from single time snapshot with the superposition of many individual unfolded band structures,

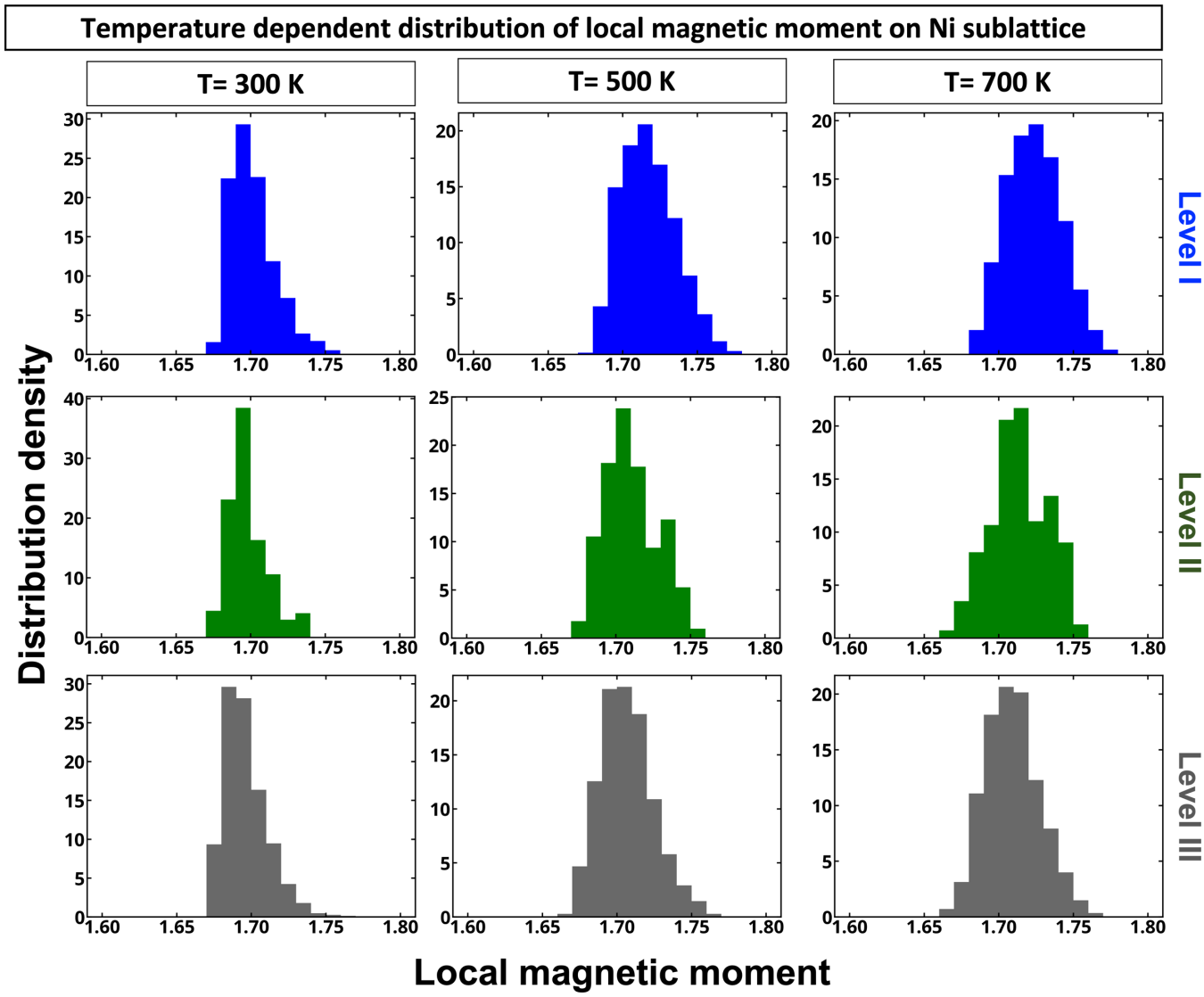

FIG. 3. Distribution of local density functional theory (DFT) magnetic moments (i.e., $\mu_i = \sqrt{\mu_{i,x}^2 + \mu_{i,y}^2 + \mu_{i,z}^2}$) on Ni corresponding to different levels of spin-lattice dynamics and different temperatures.

we find that the band structure superposition shows clearer incoherent features (or fuzziness or E-vs-k nondispersiveness) than the single unfolded band structure but almost identical coherent features (or sharpness or E-vs-k dispersiveness). The gap values extracted from the unfolded band structure are consistent with the gap from the DOS, showing a decrease in the gap of 0.3–0.5 eV going from 300 to 700 K, depending on the theory level.

According to these findings, we achieved two conclusions: Static mean-field-like DFT is sufficient to capture the properties of Mott insulators such as NiO, including the existence of an insulating gap and local magnetization, provided that the spin and lattice symmetry-breaking DOFs are considered; our *ab initio*, general, joint description of Mott insulator dynamics under finite temperature predicts that the spin and lattice dynamics, as well as their coupling, can have very different contributions to different observable properties, e.g., local magnetic moments and bandgap. Our joint model introduces temperature in DFT calculations via statistical mechanics and enables the calculation of finite temperature properties within the same computational tool. The three levels of theory in this paper show a significant advantage on the ability to investigate and understand the dynamics in a detailed and decoupled way.

A. Distribution of local magnetic moments

We find that, in contrast to traditional DFT calculations having single absolute values of magnetic moments at finite temperatures, NiO—both below and above the Néel temperature—has a distribution of local magnetic moments (Fig. 3). In all cases, the magnetic moments on Ni atoms are found to be $\sim$1.7 μ_B. These results thus demonstrate that, for PM NiO at finite temperature, attributing the failure of the SCLS with nonmagnetic globally averaged structure as the

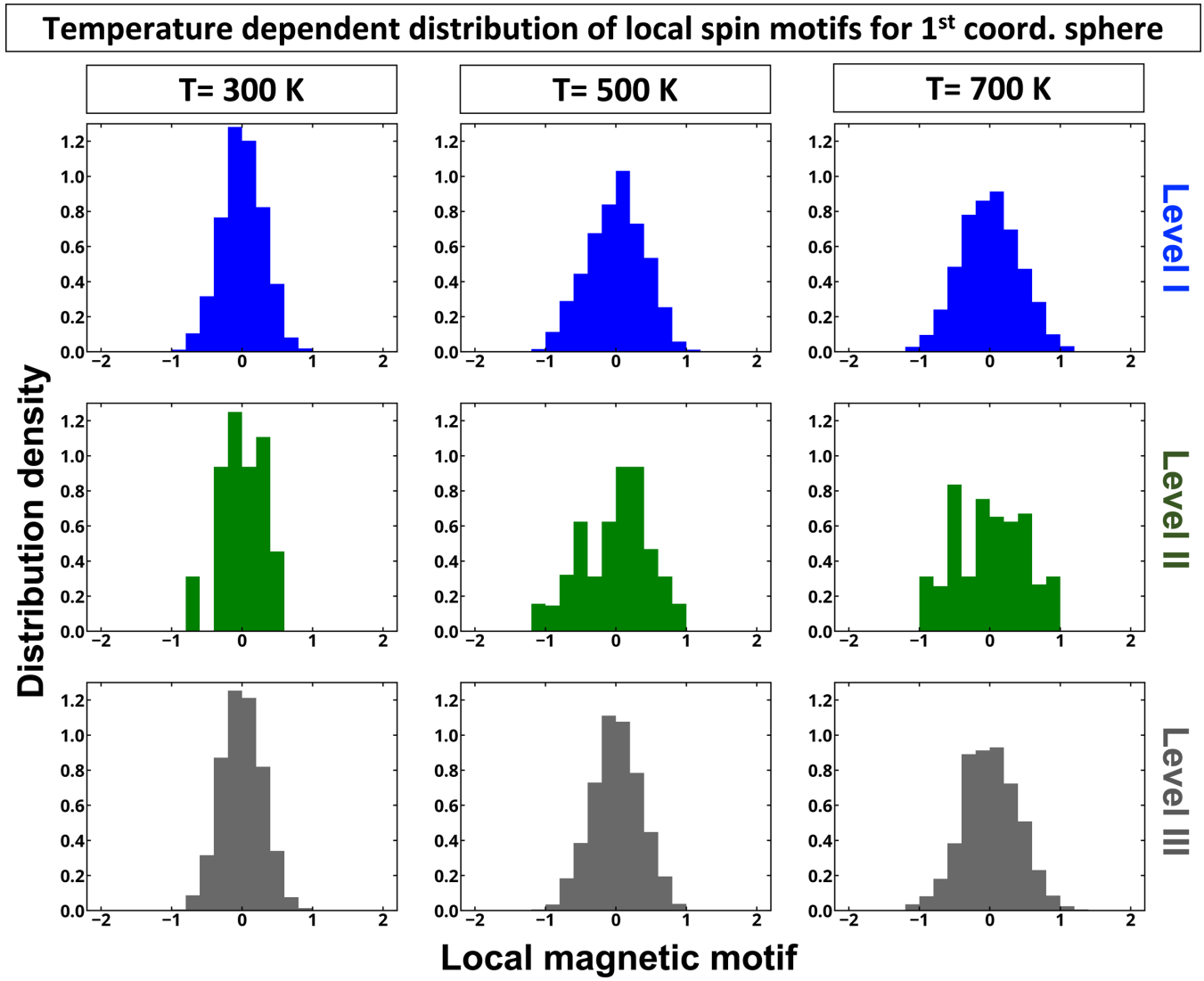

FIG. 4. Distribution of local spin motifs in the first coordination sphere for different temperatures and levels of spin-lattice dynamics.

failure of DFT, which has been claimed in many previous studies [43–45], is not fair.

Increase of temperature results in small changes in the distribution of magnetic moments, as shown in Fig. 3, which is both originated from the change of short-range spin order (discussed below) and from the different lattice constants for different temperatures. In Level II, the distribution is not as smooth as in the other two levels because only one spin configuration per temperature is employed here; therefore, each spin always maintains the same correlation with the neighboring spins, leading to a less homogenous fluctuation of the value of the local magnetic moment.

B. Distribution of LSMs

We perform detailed analysis of LSMs within the first and second coordination spheres calculated with Eq. (4). The results for different levels of spin-lattice dynamics summarized in Figs. 4 and 5 show that temperature results in a substantial broadening of the distribution of LSMs. This is especially visible for the first-coordination sphere (Fig. 4). The analysis of local spin distribution in the second coordination shells suggests significant asymmetry of the distribution at temperatures below the Néel temperature, which is caused by presence of spin ordering in the second coordination sphere. However, as temperature increases, the spins become more randomly oriented, shifting toward a Gaussian-like distribution. A residual asymmetry in the distribution for the second coordination shell at high temperature is observed at all levels. From a physical point of view, these results demonstrate that NiO has a degree of AFM correlations which survives even above the Néel temperature, and this degree reduces as temperature increases. Although qualitatively similar, the distribution of LSMs slightly differs for the different levels of spin-lattice dynamics, as illustrated in Fig. 5. Concerning Level II, the reason for the nonsmooth distribution, as previously mentioned, is due to the employment of a fixed spin configuration at each temperature, therefore, fixing the local magnetic environment and not allowing for a complete sampling of the phase space of these quantities.

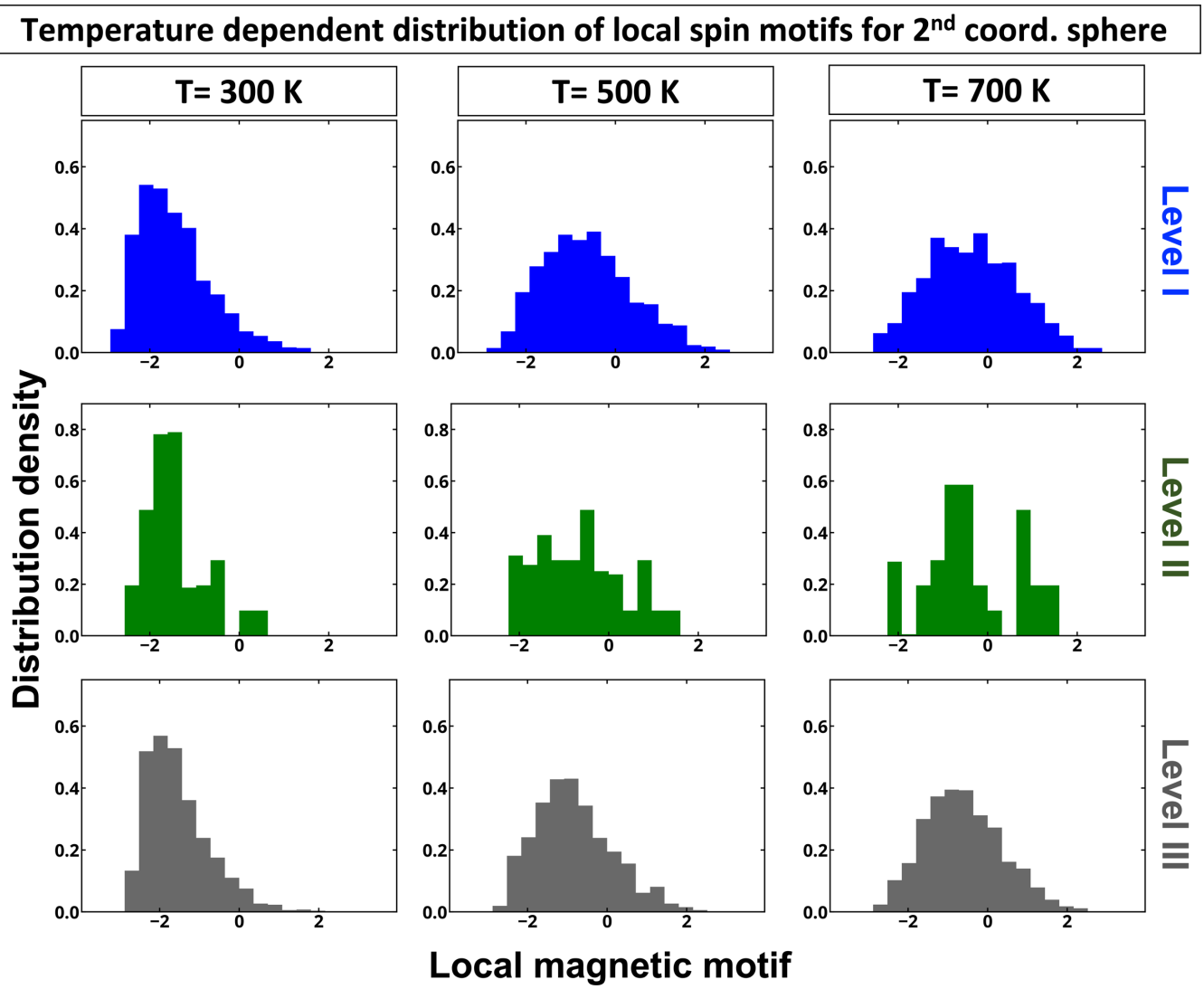

FIG. 5. Distribution of local spin motifs in the second coordination sphere for different temperatures and levels of spin-lattice dynamics.

C. Temperature dependence of SRO

The temperature dependence of distribution of local magnetic motifs is generalized in the corresponding dependence of SRO calculated using Eq (5) and shown in Fig. 6 for the first and second coordination spheres. It is found that, for the first

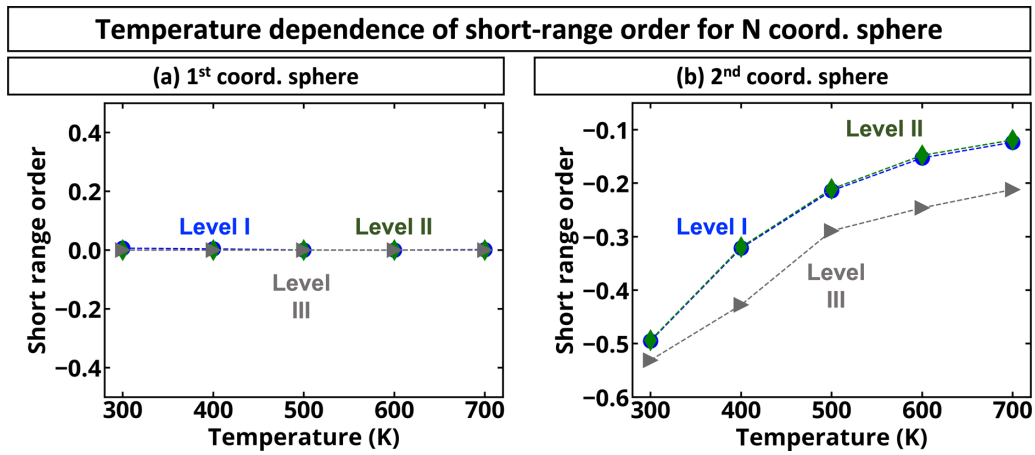

FIG. 6. Spin short-range order computed as the mean value of distribution of local spin motif for (a) first and (b) second coordination spheres as a function of temperature for different levels of spin-lattice dynamics.

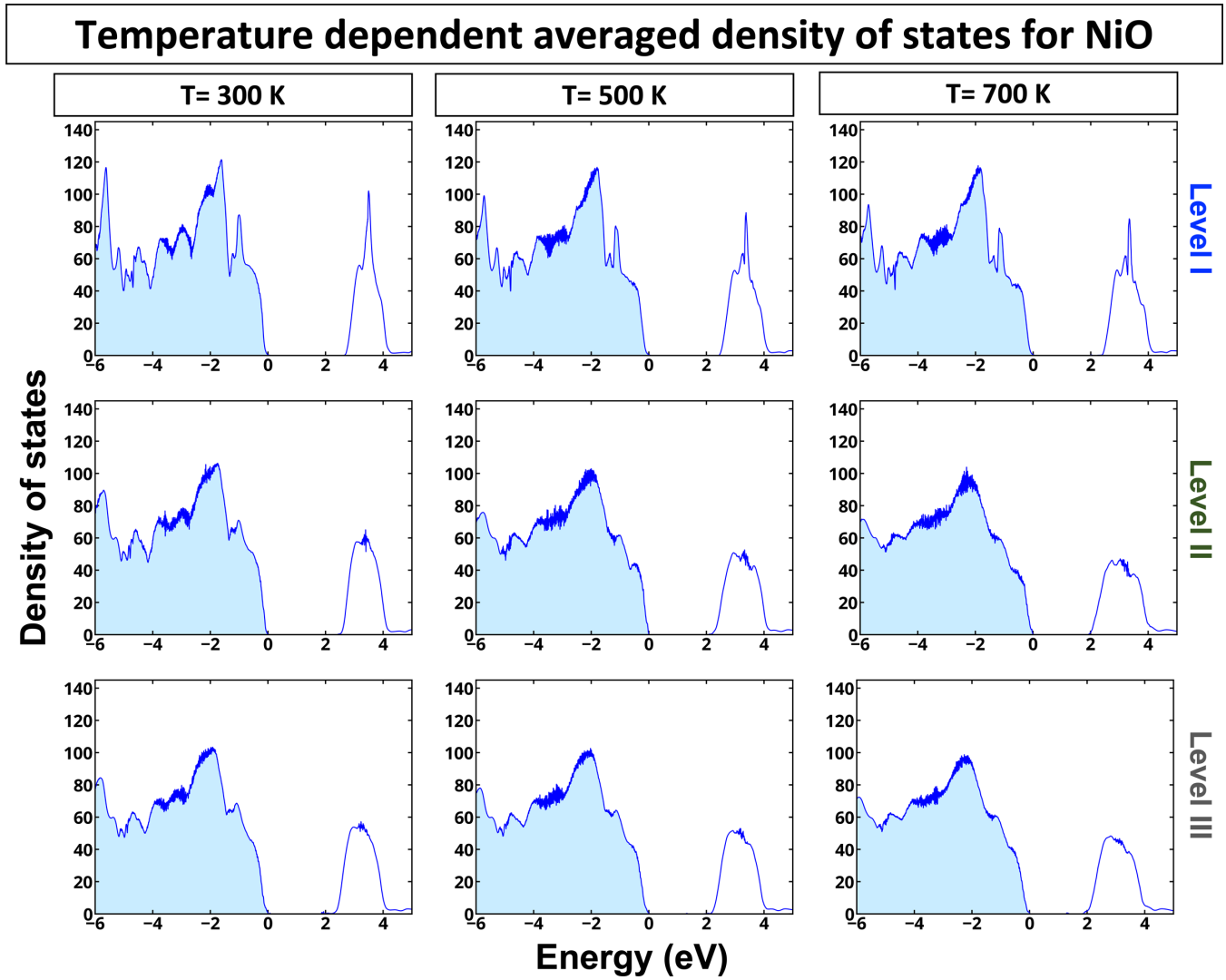

FIG. 7. Density of states averaged over snapshots for NiO computed for different levels of spin-lattice dynamics at different temperatures. The occupied states are shown by light blue shaded region.

coordination shell, the three levels agree completely with each other, with SRO = 0, as expected from the low-temperature AFM ordering of NiO and the low intensity of the exchange interactions between Ni first nearest neighbors. For the second coordination sphere, the SRO from Levels I and II are almost identical by construction since the spin configurations in Level II are chosen to match the SRO of the noncollinear Heisenberg MC of Level I. Level III, instead, shows a slightly more negative value of SRO, especially at higher temperatures. This difference is rooted in numerical resolution effects originating in the small simulation cell used in the LLG dynamics as compared with standard spin dynamics simulations (see Appendix F). However, physical mechanisms that could arise and introduce differences in the SRO parameter are the explicit accounting of spin dynamics and accounting for distance dependence of J_{ij} (not considered in Level I–II theories).

Nonetheless, in addition to supercell size convergence effects, the three levels qualitatively agree with each other and show a residual AFM correlation between Ni second nearest neighbors also at the highest temperature of 700 K. Importantly, independent of the level of spin-lattice dynamics, even below the Néel temperature, we find that AFM NiO cannot be described as a perfectly long-range ordered AFM structure but already exhibits spin symmetry breaking. This spin symmetry breaking is further enhanced above the Néel temperature.

D. Electronic structure, DOS, gaps, and unfolded band structure

1. Temperature dependence of DOS

Spin-lattice dynamics also significantly affects the electronic properties, as shown in Fig. 7. Importantly, in contrast to naïve DFT calculation, all three levels of theory predict PM NiO to be an insulator with large bandgap energy. These results are consistent with that found based on the spin-special quasirandom structure (SQS) [46,47] model (high-temperature limit of PMs) used previously [39,48], further confirming that electronic properties of PMs cannot be described as properties of global average nonmagnetic structures but should indeed be predicted as average properties of different local motifs. For all three levels of spin-lattice dynamics, we find that bandgap energies decrease with tem-

TABLE II. Bandgaps in energy and momentum, extracted from EBS with spectral function intensity > 0.1 Å eV^{-1} atom^{-1} for AFM, SQS, and Levels I, II, and III as a function of temperature. L-45%-Γ means that the band edge is along the L-Γ path having a distance to L 45% of the distance from L-Γ. All momenta are in the primitive Brillouin zone of single-cell rock salt NiO.

	Gap energy (eV)		Momentum (VBM to CBM)			
AFM ($T = 0$)	2.9		L-45%-Γ to Γ-40%-X			
SQS-PM (inf. T)	2.42		L to Γ			
	Level I		Level II		Level III	
T (K)	Gap energy (eV)	Momentum (VBM to CBM)	Gap energy (eV)	Momentum (VBM to CBM)	Gap energy (eV)	Momentum (VBM to CBM)
300	2.74	L-20%-Γ to Γ	2.6	L-38%-Γ to Γ	2.58	L-41%-Γ to Γ-45%-X
400	2.5	L-15%-Γ to Γ	2.44	L to Γ	2.50	L-38%-Γ to Γ
500	2.5	L to Γ	2.28	L to Γ	2.38	L-10%-Γ to Γ
600	2.38	L to Γ	2.12	L to Γ	2.30	L to Γ
700	2.42	L to Γ	2.08	L to Γ	2.18	L-26%-Γ to Γ

perature. This decrease is the smallest for Level I spin dynamics. This is not surprising, as Level I theory ignores the effect of thermal atomic vibration on electronic structure, which is known to reduce the bandgap energy in oxides [49] and can be seen by comparison of the results for Levels I and II theories. When comparing DOSs for Levels II and III spin-lattice dynamics, one clearly sees similarities in the electronic structures. The main difference here is only in relative intensities of the states at the band edges.

Comparing the present results with x-ray photoelectron spectroscopy measurements [50], we observe that inclusion of spin DOFs, together with the details of the employed PBE + U functional, shows improvements with respect to previous LDA + U results [51] concerning the DOS between -3 and 0 eV: The depression of DOS seen in LDA + U [51] is absent in the present results, and a peak is observed around the same energy (-2 eV) as in experiments [50]. The spectral weight of the two peaks closer to the valence band, however, is reversed as compared with the experimental spectra [50] and previous LDA + DMFT results [45], as expected in a mean-field DFT picture. Nonetheless, a detailed comparison with experiments and higher-level theories is beyond the scope of this paper since accurate results would require a careful choice of the U parameter.

2. *Temperature dependence of EBS*

The unfolded band structures for all levels at temperatures of 300, 500, and 700 K (Fig. 8) show that the temperature does not affect the sharpness or fuzziness of the bands. The only effect which can be seen is the change of absolute bandgap value. As a comparison, the EBSs for the AFM ground state [Fig. 8(a)] and for two different models of the PM state [Figs. 8(b) and 8(c)] are also shown. It is clear from Fig. 8(b) that the nonmagnetic approach does not represent the PM state of NiO, leading to a metallic band structure.

3. *Temperature dependence of bandgap energy*

Analysis of both DOS and unfolded band structure demonstrates that the increase of temperature reduces bandgap energy (Fig. 9). At Level I dynamics, the change of bandgap energy comes only from the lattice expansion and change of SRO. The Levels II and III dynamics clearly show lower bandgap energies than Level I, which is mainly because of thermally induced atomic displacements on bandgap energy that are accounted in Level II/III dynamics but not accounted in Level I dynamics. When comparing the bandgap difference for Levels II and III spin dynamics, we conclude that this difference is within the error bar of calculations and results in identical bandgap energies. We note that the gap values extracted from DOS and EBS are consistent with each other. In Table II, the bandgap energy for AFM, SQS, and the three levels of theory for all temperatures investigated are presented, together with the position in momentum of the valence band maximum (VBM) and the conduction band minimum (CBM).

V. CONCLUSIONS

In this paper, we have simulated across the Néel transition temperature an AFM insulator using three levels of increasing complexity in accounting for spin and lattice excitations and their dynamics. The treatment of electron-electron interactions, on the other hand, is kept on the mean-field DFT level. Our methodologies allow us to reaffirm the findings in our previous works [14–16,49,52–57] that the mean-field DFT level of theory is very capable of correctly predict the existence of an electronic gap also in the PM phase, if one avoids the naïve single-site averaging of magnetic fluctuations into a nonmagnetic solution. Instead, gapping appears when the PM state is modeled as a disordered magnetic state.

With this knowledge at hand, we can make use of the efficiency of DFT to probe the question of how a disordered magnetic state behaves dynamically, how it interacts with lattice vibrations, and how such DOFs manifest in the electronic structure.

We demonstrate these effects by performing simulations on three different levels of dynamics: (I) Only the spin state is dynamic, while the lattice is kept frozen on ideal points. (II) A subset of the snapshot of the magnetic states obtained in (I) is kept fixed, while the lattice is dynamically simulated using AIMD. Finally, in (III), we used LLG atomic spin dynamics

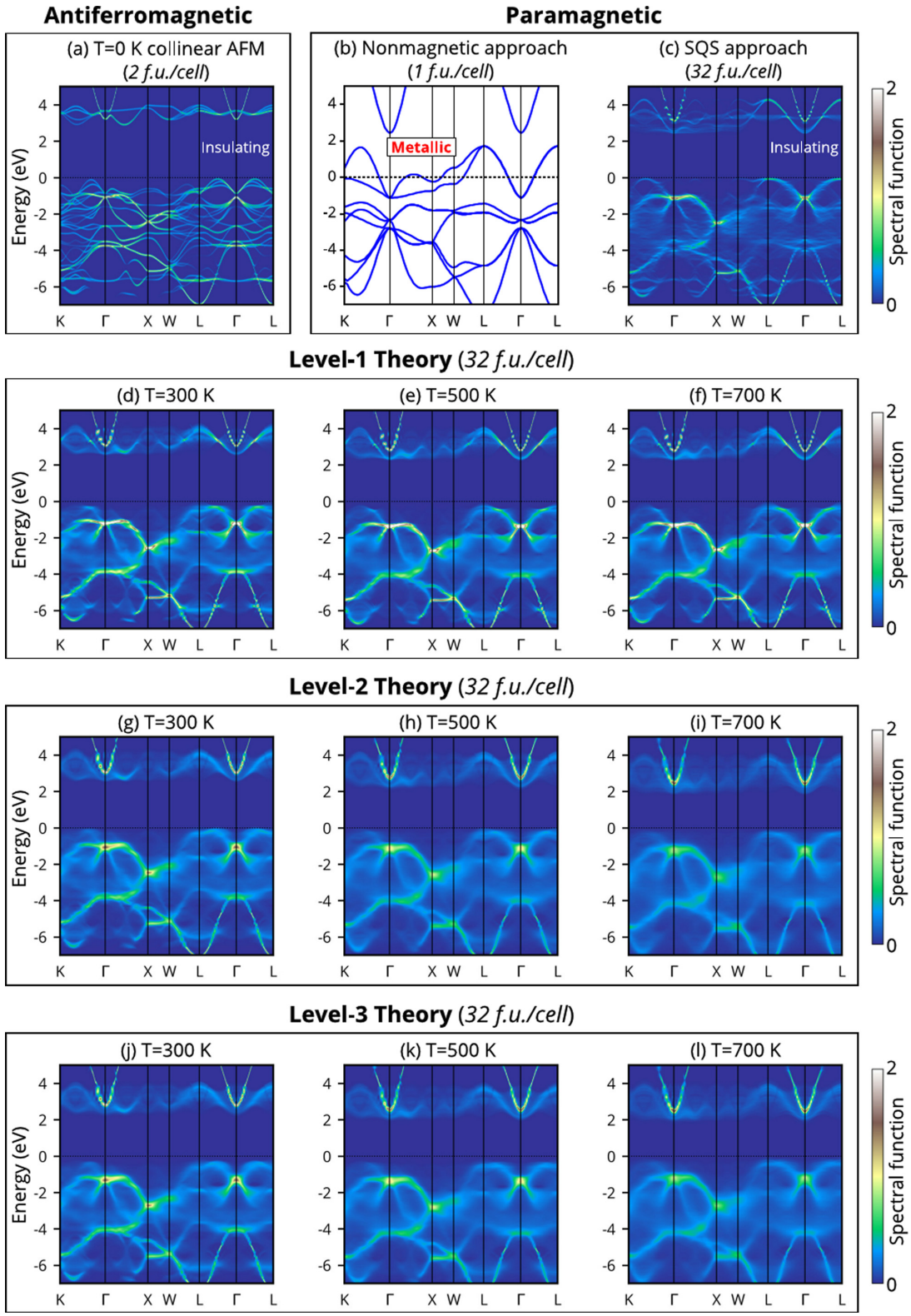

FIG. 8. NiO band structure from different levels of theory. (a) The unfolded effective band structure (EBS) obtained by density functional theory (DFT) + U using a $T = 0$ collinear antiferromagnetic double-cell structure (2 f.u./cell), unfolded back into the primitive Brillouin zone, showing an insulating gap. (b) The band structure obtained by the same DFT + U method but using the nonmagnetic approach of the paramagnetic phase, showing no gap, hence a metallic behavior. (c) EBS obtained by the same DFT + U method but using the magnetic special quasirandom structure (SQS) supercell approach, which shows a gap like (a). The last three rows show the EBS obtained by the same DFT + U method, using lattice and spin structures from (d)–(f) Level I, (g)–(i) Level II, and (j)–(l) Level III theories at three different temperatures.

coupled with AIMD to simulate a dynamically coupled spin and lattice state.

Our focus is on the electronic consequences of these levels of dynamics. We find that the effect of lattice vibrations and spin dynamics affects the EMPs of the system under investigation, and both effects should be considered at some level to obtain a full picture of the system. In Level III, we only observe minute differences from Level II in terms of DOS-derived bandgaps, but a somewhat larger difference is seen when evaluating the bandgap with the EBS-based method. This indicates that the electronic states in the vicinity of the band edges demonstrate some influence of the coupled dynamics even if the absolute band edge positions do not. Overall, however, we conclude that, for PM NiO, the important aspect in theoretical modeling is to consider disordered magnetism and lattice vibrations. The effect of their mutual dynamical coupling is not large on the properties studied here. Further investigations could be directed to properties such as phonon lifetimes, thermal conductivity, and other aspects where dynamical phenomena can have a larger impact.

ACKNOWLEDGMENTS

BA acknowledges funding from the Swedish Foundation for Strategic Research through the Future Research Leaders 6 program, Grant No. FFL 15-0290, from the Swedish Research Council (VR) through Grant No. 2019-05403, and from the Knut and Alice Wallenberg Foundation (Wallenberg Scholar Grant No. KAW-2018.0194), and the support from the Swedish Government Strategic Research Area in Materials Science on Functional Materials at Linköping University (Faculty Grant SFOMatLiU No. 2009 00971). Part of the computations were enabled by resources provided by the Swedish National Infrastructure for Computing at the National Supercomputer Centre partially funded by the Swedish Research Council through Grant Agreement No. 2018-05973. The work of AZ, OM, and ZW at the Colorado University, Boulder, was supported by U.S. National Science Foundation, Division of Materials Research (DMR), Condensed Matter and Materials Theory Grant No. DMR 2113922 and utilized the Extreme Science and Engineering Discovery Environment supercomputer resources, which are supported by the National Science Foundation Grant No. ACI-1548562.

APPENDIX A: ANALYSIS OF SPIN AND VIBRATIONAL TIMESCALES

Spin-lattice coupling has been discussed for NiO experimentally [18–21] as the reason for the anomalous shift of the two-magnon peak with temperatures across the Néel temperature. This implies that the spin-lattice coupling could lead to changes in properties as a function of temperature. However, such a coupling has been neglected in previous theoretical works. We investigate the spin and vibrational timescales as a preliminary step to motivate our three-level investigation. This is done below the Néel temperature in the AFM magnetic phase.

To do so, we calculate the spin autocorrelation function from an ASD simulation with exchange interactions from Level I and, separately, the velocity autocorrelation function from an AIMD simulation, which corresponds to Level II of Fig. 1. Both simulations are carried out at 300 K in the AFM state ($T_N = 320$ K, see Appendix B), using a 32 f.u. supercell. In the ASD simulation, we use a timestep of 0.01 fs, and we run the simulation for 10 ps. The AIMD simulation is taken from level II, see Appendix C for computational details. The autocorrelation function $C(t)$ at time lag t is defined as

$$C(t) = \left\langle \frac{1}{N_{\text{atoms}}} \sum_{i=1}^{N_{\text{atoms}}} \mathbf{a}_i(t_0) \cdot \mathbf{a}_i(t_0 + t) \right\rangle_{t_0},$$

where $\mathbf{a}_i$ is the vector quantity under investigation (spin or atomic velocity) related to atom i, and the average is performed over time origins t_0. The two separate simulations allow us to investigate the timescales independently of each other, from which the possible coupling can then be judged. The results are presented in Fig. 10.

From Fig. 10, one can notice that the velocity autocorrelation function falls off slower than that of the spins. However, the difference in the decreasing speed (that can present the timescale) is not orders of magnitude but rather a factor of 4 since the spin and the velocity autocorrelation functions decrease from 1.0 to 0.2 in ∼20 and 80 fs, respectively. This relation suggests that one could find a nonnegligible effect of spin-lattice coupling for some properties if employing a simulation technique that considers an interaction between spin and lattice DOFs, such as the Level III theory in this paper.

TABLE III. Exchange interactions $J_{ij}^{(s)}$ from DFT cluster expansion inversion method employing shells of up to second and eighth nearest neighbors. The superscript (s) in the exchange interactions $J_{ij}^{(s)}$ indicates the interaction shell. All values are in millielectronvolts.

Exchange energy	Shell of up to second nearest neighbors	Shell of up to eighth nearest neighbors
$J_{ij}^{(1)}$	0.865	0.865
$J_{ij}^{(2)}$	−9.54	−9.54
$J_{ij}^{(3)}$	–	−0.1
$J_{ij}^{(4)}$	–	−0.2
$J_{ij}^{(5)}$	–	0.0
$J_{ij}^{(6)}$	–	0.0
$J_{ij}^{(7)}$	–	0.0
$J_{ij}^{(8)}$	–	−0.2

APPENDIX B: LEVEL I DYNAMICS: OBTAINING THE HEISENBERG EXCHANGE INTERACTIONS FROM DFT; MC DETAILS AND COMPARING T_N WITH LITERATURE

Results for $J_{ij}^{(s)}$, where s indicates the coordination shell, are shown in Table III. Since exchange interactions between farther coordination shells are extremely small and induce differences of the order of ∼10% in the prediction of the Néel temperature, with negligible improvement, herein, we considered exchange interactions up to the second coordination shell with $J_{ij}^{(1)} = 0.865$ meV and $J_{ij}^{(2)} = -9.54$ meV (the same as those shown by Zhang *et al.* [58]). We note that an

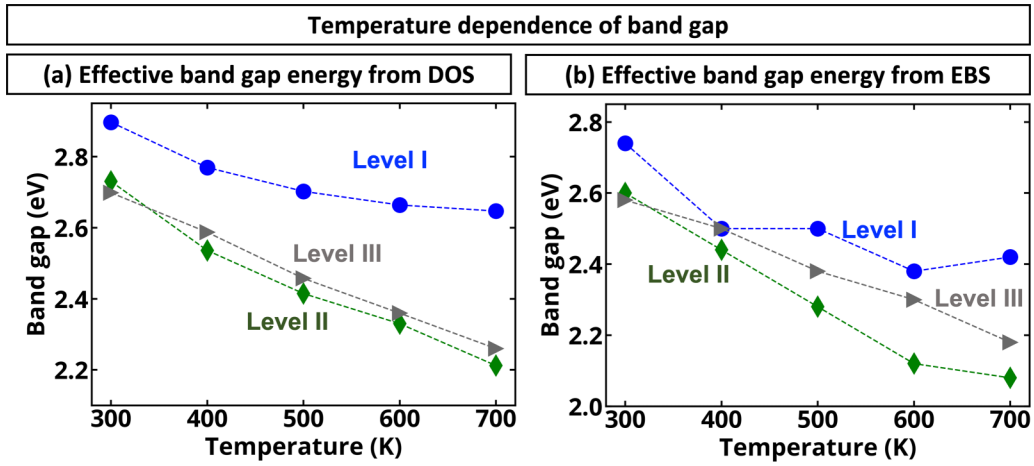

FIG. 9. Temperature dependence of bandgap energy calculated for different levels of lattice-spin dynamics computed using (a) averaged density of states (DOS) and (b) unfolded band structure approach. For DOS, the bandgap is calculated between occupied and unoccupied states having intensity of 0.1 eV^{-1} $atom^{-1}$. Bandgaps in energy and momentum are extracted from effective band structure (EBS) with spectral function intensity >0.1 Å eV^{-1} $atom^{-1}$.

alternative approach to extract exchange energies from DFT is to determine them by small-angle rotations: The linear-response theory provides the exchange energies appropriate to small-angle spin rotations, as required by the Heisenberg representation, thus avoiding the approximation [59,60] of obtaining J_{ij} from purely ferromagnetic and purely AFM large-angle spin rotations. These were used, for example, in Ref. [61] to calculate by MC the Heisenberg problem in GaAsMn.

1. MC simulations of spin configurations and the Néel phase transition

MC simulations were run with the UPPASD code [4,62] using 2 and 10 repetitions in all x, y, and z directions (32 and 4000 f.u., respectively) of the conventional face-centered cubic NiO cell (only Ni atoms are magnetic). The different supercell sizes are employed to quantize the finite-sized errors. At each temperature, the system is first thermalized carrying out 100 000 (10 000) MC steps with the small (large) supercell. The measurement phase consisted of an additional 1 000 000 (20 000) MC steps in the small (large) supercell. Note that, in the MC simulations, we do not consider the dependence of J_{ij} on lattice constant, and hence, the effect of lattice expansion on the spin DOF is neglected. This approximation is motivated by the fact that lattice expansion in the considered temperature range leads to changes in the exchange interactions smaller or equal to 0.2 meV, which does not have any appreciable effect on transition temperature and SRO parameter.

Around the peak of the specific heat (see Fig. 11), MC simulations are carried out every 10 K to have a higher resolution of the transition temperature (i.e., 10 K can also be seen as our error bar in the calculation of T_N). We find that, despite that the two supercell sizes have noticeable difference in the temperature

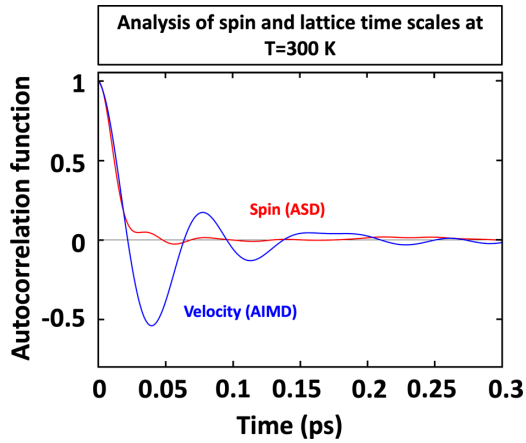

FIG. 10. Spin (red) and velocity (blue) autocorrelation functions in the antiferromagnetic (AFM) state at $T = 300$ K, as an example, from uncoupled atomistic spin dynamics (ASD; like Level I) and uncoupled *ab initio* molecular dynamics (AIMD; Level II), respectively.

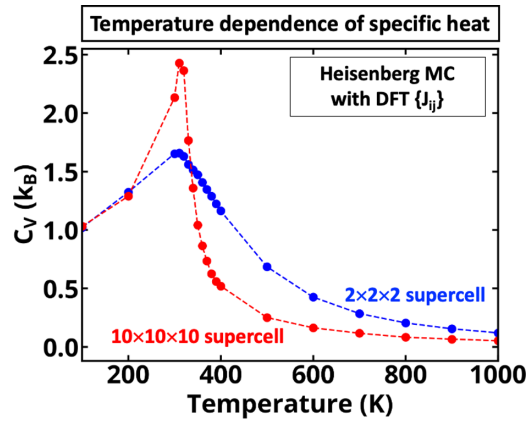

FIG. 11. Specific heat from Heisenberg Monte Carlo simulations for 2 × 2 × 2 and 10 × 10 × 10 supercells. The predicted Néel temperature is ∼320 K. Dashed lines are just a guide to the eye.

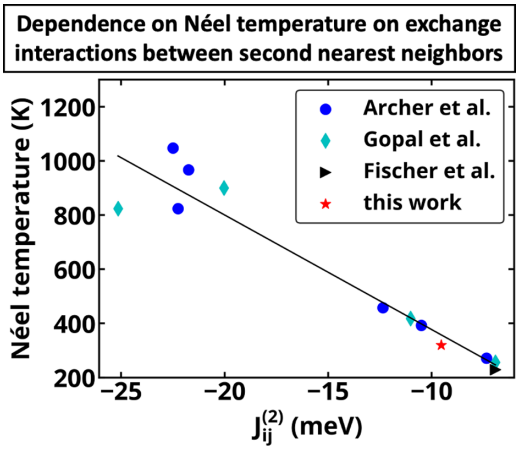

FIG. 12. Comparison of T_N as a function of $J_{ij}^{(2)}$ from Monte Carlo (MC) simulations from different works [63–65] (see Table IV and corresponding $J_{ij}^{(1)}$ values shown there). $J_{ij}^{(2)}$ and T_N from the works are rescaled to be consistent, i.e., having the same definition of exchange interactions and neglecting quantum corrections on the moment sizes (see correction in Fischer *et al.* [64]).

profile of the specific heat, both 32 and 32 000 f.u. Heisenberg MC calculations result in the same Néel temperature of ∼320 K (Ising Hamiltonian simulations via the collinear MC method have also been carried out, and the predicted Néel temperature is 980 K), which is substantially smaller than the experimentally known Néel temperature of 523 K [17]. These results are consistent with other Heisenberg MC simulations in the literature [63–65]. An alternative method [66] to determine the Néel temperature requires the fourth moment of the order parameter for different sizes of the simulation box as a function of temperature: These curves all cross at the same temperature, which is the critical temperature. This method, employed, for example, in Ref. [61], is more accurate in the determination of the transition temperature than the inspection of the specific heat curve; however, in this paper, we are not after accurate Néel temperatures since we are already aware of the issues of the Heisenberg Hamiltonian in the prediction of transition temperatures in antiferromagnets.

2. Comparison of $J_{ij}^{(2)}$ and T_N used in this paper and reported in the literature

Figure 12 and Table IV provide the summary of the computed $J_{ij}^{(2)}$ and T_N in this paper and that reported in the literature [63–65]. The underestimation of the transition temperature is common in the transition metal oxide series MnO, FeO, CoO, and NiO, as seen in Ref. [64], where both the cluster expansion method and the magnetic force theorem [59] were used and showed minor differences in the values of the exchange interactions. Exchange interactions calculated with the advanced functional in Ref. [65] showed a better agreement, although employment of the classical Heisenberg Hamiltonian could also be responsible for the underestimation.

APPENDIX C: LEVEL II DYNAMICS: DETAILS OF AIMD

The AIMD simulations were carried out using noncollinear PBE + U calculations [32,33] with U of 5 eV applied to Ni-d states as implemented in VASP [34–37] at temperatures from 300 to 700 K in steps of 100 K with a $2 \times 2 \times 2$ supercell (32 f.u.) using a fixed magnetic configuration with the SRO parameter as close as possible to the results of the MC simulations of Level I at the corresponding temperature. The simulations are run in the canonical ensemble using Langevin dynamics with a friction parameter of 10 ps^{-1}. At each temperature, we run for ∼2 ps, disregarding the first 0.5 ps as thermalization. The snapshots on which we calculate DOS and band structure are separated from each other by ∼100 fs. The lattice constants of NiO were changed gradually from 4.179 to 4.201 Å corresponding to 300 and 700 K AIMD calculations, respectively, according to the experimental thermal expansion [31]. The cutoff energy was fixed to 600 eV, and the Brillouin zone is sampled using a $2 \times 2 \times 2$ Γ-centered Monkhorst-Pack grid [38].

TABLE IV. Exchange interactions and predicted Néel temperature for Heisenberg Hamiltonian from this paper and previous works [63–65]. The values of exchange interactions can differ greatly even using the same exchange and correlation functional because of the value of U employed. All exchange interactions $J_{ij}^{(s)}$ and T_N are rescaled to agree with the present formulation of the Heisenberg Hamiltonian and without accounting for quantum corrections.

Method	$J_{ij}^{(1)}$ (meV)	$J_{ij}^{(2)}$ (meV)	T_N (K)
This paper, PBE + U	0.865	−9.54	320
LDA-PW [63]	−0.25	−7.35	272
LDA-localized orbitals [63]	2.7	−21.75	967
PBE [63]	0.6	−22.25	824
PSIC [63]	1.65	−12.35	458
HSE [63]	1.15	−10.5	393
ASIC [63]	2.6	−22.5	1048
SIC-LSDA [64]	0.15	−6.92	229
LDA + U [65]	1.48	−20.035	900
PBE + U [65]	2.355	−25.15	824
ABCN0-LDA [65]	1.015	−11.015	418
ABCN0-PBE [65]	0.4	−6.925	256

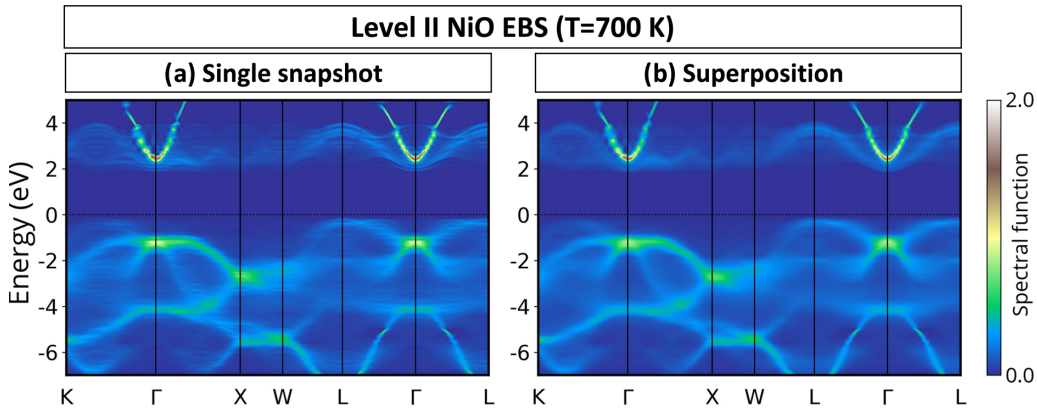

FIG. 13. For $T = 700$ K, noncollinear spin level-2 $2 \times 2 \times 2$ (32 f.u.) supercell, (a) effective band structure (EBS) of a single snapshot (index = 506), and (b) the superposition of 10 EBSs of 10 snapshots (index = 506–2108). The energy zeros in the figure are the location of supercell valence band maximum (VBM; before unfolding). The sharp bands from +2 to higher energy are from Ni *s* orbitals, while Ni *d* electrons dominate the fuzzy bands from −6 to 0 eV. The superposition, or time average, smoothens the EBS but does not introduce any other changes. This is true for all levela of EBSs of all temperatures calculated.

APPENDIX D: DISTANCE-DEPENDENT EXCHANGE INTERACTIONS

The distance-dependent exchange interactions, as described in Ref. [23], are obtained by calculating the exchange interactions between pairs of moments in lattice configurations with consistent thermal atomic displacements. To generate these configurations, we ran an ASD-AIMD simulation with fixed exchange interactions from Table III with a $3 \times 3 \times 3$ supercell at 700 K. From this simulation, we extracted three snapshots in which we selected several pairs of moments with different interatomic distances. The exchange interaction for a particular pair of moments i and j are then obtained by carrying out total energy DFT calculations with the moments i-j in configuration up-up, up-down, down-up, and down-down, while keeping frozen the magnetic moments on all other atoms. The J_{ij} between moment i and j are finally calculated as

$$J_{ij} = -\tfrac{1}{8}[E(\uparrow\uparrow) + E(\downarrow\downarrow) - E(\downarrow\uparrow) - E(\uparrow\downarrow)], \qquad (8)$$

where $E(\uparrow\uparrow)$ indicates the total energy of the supercell with both spin i and j pointing up and correspondingly for the other energies. The resulting exchange interactions are shown in Fig. 2.

APPENDIX E: EXTENDED BAND STRUCTURE CALCULATIONS

The superposition of different snapshots, or time average, smoothens the EBS but does not introduce any other changes. This is true for all levels of EBS of all temperatures calculated. This can be seen in Fig. 13, where examples of EBS from a

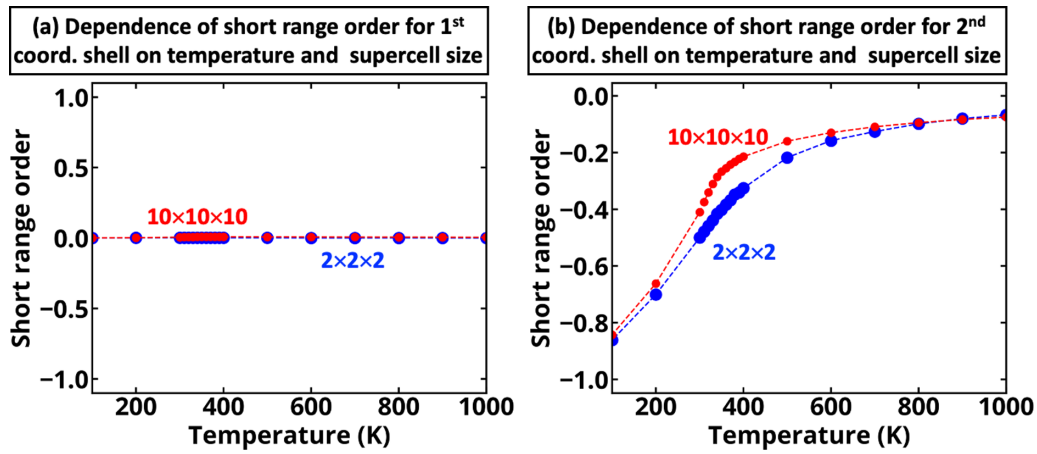

FIG. 14. Short-range order (SRO) parameter for second nearest neighbors from Heisenberg Monte Carlo (MC) simulations for different cells. The vertical red line indicates the predicted Néel temperature. The results show a considerable finite size effect, with the $2 \times 2 \times 2$ supercell overestimating the strength of SRO at temperatures just above T_N. In Heisenberg MC simulations, the size of the magnetic moments is considered fixed to the value obtained in the ground state (1.7 μ_B); therefore, the SRO is calculated for unit vectors such that antiferromagnetic (AFM) ordering corresponds to SRO = −1.

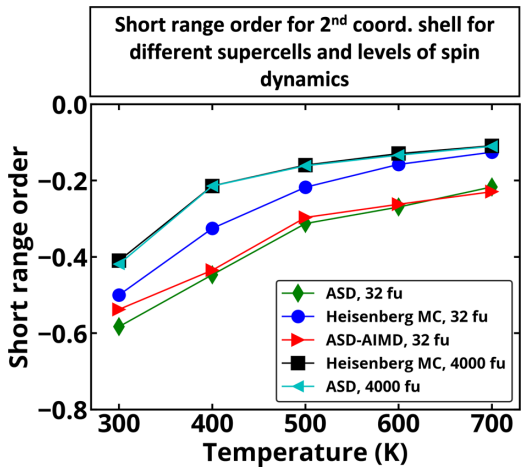

FIG. 15. Short-range order (SRO) from two Heisenberg Monte Carlo (MC) simulations, with a $2 \times 2 \times 2$ supercell (32 f.u., blue circles) and a $10 \times 10 \times 10$ supercell (4000 f.u., black squares), together with the SRO from two atomistic spin dynamics (ASD) simulations, with the same cell sizes (32 f.u.: green diamond; 4000 f.u.: left-pointing cyan triangle) and from combined atomistic spin dynamics - *ab initio* molecular dynamics (ASD-AIMD; 32 f.u. right-pointing red triangle), which corresponds to Level III. MC and ASD simulations are run with the exchange interactions calculated on ideal lattice; the ASD-AIMD simulation is carried out instead using the distance-dependent J (first and second shells, Fig. 2).

single snapshot [Fig. 13(a)] and the superposition [Fig. 13(b)] for Level II at 700 K are presented.

APPENDIX F: SRO FROM MC AND ASD CALCULATIONS

SRO parameters for the first and second coordination shells from MC are shown in Fig. 14 for supercell sizes of $2 \times 2 \times 2$ and $10 \times 10 \times 10$ repetitions. SRO for the first coordination shell is zero for all temperatures and cells employed, whereas for the second coordination shell, a considerable finite-sized effect is observed around the Néel temperature, with the $2 \times 2 \times 2$ cell overestimating the strength of SRO. This finite-sized effect is even more pronounced in ASD, as shown in Fig. 15. In this figure, we see that the large cell ($10 \times 10 \times 10$, 4000 f.u.) MC and ASD results (black squares and cyan left-pointing triangles, respectively) agree perfectly, whereas for the smaller cell ($2 \times 2 \times 2$, 32 f.u.), there is a considerable difference between MC (blue circles) and ASD (green diamonds). The ASD-AIMD simulations (red right-pointing triangle) inherit this finite-sized effect.

[1] E. Beaurepaire, J.-C. Merle, A. Daunois, and J.-Y. Bigot, Ultrafast Spin Dynamics in Ferromagnetic Nickel, Phys. Rev. Lett. **76**, 4250 (1996).

[2] B. Koopmans, J. J. M. Ruigrok, F. D. Longa, and W. J. M. de Jonge, Unifying Ultrafast Magnetization Dynamics, Phys. Rev. Lett. **95**, 267207 (2005).

[3] M. Djordjevic and M. Münzenberg, Connecting the timescales in picosecond remagnetization experiments, Phys. Rev. B **75**, 012404 (2007).

[4] O. Eriksson, A. Bergman, L. Bergqvist, and J. Hellsvik, *Atomistic Spin Dynamics: Foundations and Applications* (Oxford University Press, Oxford, 2017).

[5] B. Koopmans, G. Malinowski, F. Dalla Longa, D. Steiauf, M. Fähnle, T. Roth, M. Cinchetti, and M. Aeschlimann, Explaining the paradoxical diversity of ultrafast laser-induced demagnetization, Nat. Mater. **9**, 259 (2010).

[6] R. J. Elliott, Theory of the effect of spin-orbit coupling on magnetic resonance in some semiconductors, Phys. Rev. **96**, 266 (1954).

[7] Y. Yafet, g factors and spin-lattice relaxation of conduction electrons, Solid State Physics **14**, 1 (1963).

[8] L. D. Landau and E. Lifshitz, On the theory of the dispersion of magnetic permeability in ferromagnetic bodies, Phys. Z. Sowjet. **8**, 153 (1935).

[9] T. L. Gilbert, A phenomenological theory of damping in ferromagnetic materials, IEEE Trans. Magn. **40**, 3443 (2004).

[10] J. Hellsvik, D. Thonig, K. Modin, D. Iuşan, A. Bergman, O. Eriksson, L. Bergqvist, and A. Delin, General method for atomistic spin-lattice dynamics with first-principles accuracy, Phys. Rev. B **99**, 104302 (2019).

[11] P.-W. Ma and S. L. Dudarev, Atomistic spin-lattice dynamics, in *Handbook of Materials Modeling*, edited by W. Andreoni and S. Yip (Springer, Cham, 2020).

[12] E. Mozafari, B. Alling, M. P. Belov, and I. A. Abrikosov, Effect of the lattice dynamics on the electronic structure of paramagnetic NiO within the disordered local moment picture, Phys. Rev. B **97**, 035152 (2018).

[13] I. Stockem, A. Bergman, A. Glensk, T. Hickel, F. Körmann, B. Grabowski, J. Neugebauer, and B. Alling, Anomalous Phonon Lifetime Shortening in Paramagnetic CrN Caused by Spin-Lattice Coupling: A Combined Spin and *Ab Initio* Molecular Dynamics Study, Phys. Rev. Lett. **121**, 125902 (2018).

[14] J. Varignon, M. Bibes, and A. Zunger, Mott gapping in 3d ABO_3 perovskites without Mott-Hubbard interelectronic repulsion energy U, Phys. Rev. B **100**, 035119 (2019).

[15] J. Varignon, M. Bibes, and A. Zunger, Origin of band gaps in 3d perovskite oxides, Nat. Commun. **10**, 1658 (2019).

[16] O. I. Malyi and A. Zunger, False metals, real insulators, and degenerate gapped metals, Appl. Phys. Rev. **7**, 41310 (2020).

[17] W. L. Roth, Magnetic structures of MnO, FeO, CoO, and NiO, Phys. Rev. **110**, 1333 (1958).

[18] R. Newman and R. M. Chrenko, Optical properties of nickel oxide, Phys. Rev. **114**, 1507 (1959).

[19] R. E. Dietz, G. I. Parisot, and A. E. Meixner, Infrared absorption and Raman scattering by two-magnon processes in NiO, Phys. Rev. B **4**, 2302 (1971).

[20] M. M. Lacerda, F. Kargar, E. Aytan, R. Samnakay, B. Debnath, J. X. Li, A. Khitun, R. K. Lake, J. Shi, and A. A. Balandin, Variable-temperature inelastic light scattering spectroscopy of

nickel oxide: disentangling phonons and magnons, Appl. Phys. Lett. **110**, 202406 (2017).
[21] E. Aytan, B. Debnath, F. Kargar, Y. Barlas, M. M. Lacerda, J. X. Li, R. K. Lake, J. Shi, and A. A. Balandin, Spin-phonon coupling in antiferromagnetic nickel oxide, Appl. Phys. Lett. **111**, 252402 (2017).
[22] S. M. Rezende, A. Azevedo, and R. L. Rodríguez-Suárez, Introduction to antiferromagnetic magnons, J. Appl. Phys. **126**, 151101 (2019).
[23] A. Lindmaa, R. Lizárraga, E. Holmström, I. A. Abrikosov, and B. Alling, Exchange interactions in paramagnetic amorphous and disordered crystalline CrN-based systems, Phys. Rev. B **88**, 054414 (2013).
[24] N. M. Rosengaard and B. Johansson, Finite-temperature study of itinerant ferromagnetism in Fe, Co, and Ni, Phys. Rev. B **55**, 14975 (1997).
[25] A. V Ruban, S. Khmelevskyi, P. Mohn, and B. Johansson, Temperature-induced longitudinal spin fluctuations in Fe and Ni, Phys. Rev. B **75**, 054402 (2007).
[26] D. Gambino, M. Arale Brännvall, A. Ehn, Y. Hedström, and B. Alling, Longitudinal spin fluctuations in bcc and liquid Fe at high temperature and pressure calculated with a supercell approach, Phys. Rev. B **102**, 014402 (2020).
[27] M. Hoffmann and S. Blügel, Systematic derivation of realistic spin models for beyond-Heisenberg solids, Phys. Rev. B **101**, 024418 (2020).
[28] X. He, N. Helbig, M. J. Verstraete, and E. Bousquet, TB2J: a python package for computing magnetic interaction parameters, Comput. Phys. Commun. **264**, 107938 (2021).
[29] C. K. Majumdar, Antiferromagnetism in the Heisenberg Hamiltonian, Bull. Mater. Sci. **3**, 209 (1981).
[30] J. W. D. Connolly and A. R. Williams, Density-functional theory applied to phase transformations in transition-metal alloys, Phys. Rev. B **27**, 5169 (1983).
[31] S. P. Srivastava, R. C. Srivastava, I. D. Singh, S. D. Pandey, and P. L. Gupta, Temperature dependence of thermal expansion and infrared lattice vibrational mode of nickel oxide, J. Phys. Soc. Japan **43**, 885 (1977).
[32] J. P. Perdew, K. Burke, and M. Ernzerhof, Generalized Gradient Approximation Made Simple, Phys. Rev. Lett. **77**, 3865 (1996).
[33] S. L. Dudarev, G. A. Botton, S. Y. Savrasov, C. J. Humphreys, and A. P. Sutton, Electron-energy-loss spectra and the structural stability of nickel oxide: an LSDA + U study, Phys. Rev. B **57**, 1505 (1998).
[34] G. Kresse and J. Hafner, *Ab initio* molecular dynamics for liquid metals, Phys. Rev. B **47**, 558 (1993).
[35] G. Kresse and J. Hafner, *Ab initio* molecular-dynamics simulation of the liquid-metal–amorphous-semiconductor transition in germanium, Phys. Rev. B **49**, 14251 (1994).
[36] G. Kresse and J. Furthmüller, Efficiency of *ab-initio* total energy calculations for metals and semiconductors using a plane-wave basis set, Comput. Mater. Sci. **6**, 15 (1996).
[37] G. Kresse and J. Furthmüller, Efficient iterative schemes for *ab initio* total-energy calculations using a plane-wave basis set, Phys. Rev. B **54**, 11169 (1996).
[38] H. J. Monkhorst and J. D. Pack, Special points for Brillouin-zone integrations, Phys. Rev. B **13**, 5188 (1976).
[39] Y. Zhang, J. Furness, R. Zhang, Z. Wang, A. Zunger, and J. Sun, Symmetry-breaking polymorphous descriptions for correlated materials without interelectronic U, Phys. Rev. B **102**, 045112 (2020).
[40] L.-W. Wang, L. Bellaiche, S.-H. Wei, and A. Zunger, "Majority Representation" of Alloy Electronic States, Phys. Rev. Lett. **80**, 4725 (1998).
[41] V. Popescu and A. Zunger, Effective Band Structure of Random Alloys, Phys. Rev. Lett. **104**, 236403 (2010).
[42] V. Popescu and A. Zunger, Extracting E versus $\vec{k}$ effective band structure from supercell calculations on alloys and impurities, Phys. Rev. B **85**, 085201 (2012).
[43] X. Ren, I. Leonov, G. Keller, M. Kollar, I. Nekrasov, and D. Vollhardt, LDA + DMFT computation of the electronic spectrum of NiO, Phys. Rev. B **74**, 195114 (2006).
[44] G. Kotliar, S. Y. Savrasov, K. Haule, V. S. Oudovenko, O. Parcollet, and C. A. Marianetti, Electronic structure calculations with dynamical mean-field theory, Rev. Mod. Phys. **78**, 865 (2006).
[45] J. Kuneš, V. I. Anisimov, A. V. Lukoyanov, and D. Vollhardt, Local correlations and hole doping in NiO: a dynamical mean-field study, Phys. Rev. B **75**, 165115 (2007).
[46] A. Zunger, S.-H. Wei, L. G. Ferreira, and J. E. Bernard, Special Quasirandom Structures, Phys. Rev. Lett. **65**, 353 (1990).
[47] S.-H. Wei, L. G. Ferreira, J. E. Bernard, and A. Zunger, Electronic properties of random alloys: special quasirandom structures, Phys. Rev. B **42**, 9622 (1990).
[48] G. Trimarchi, Z. Wang, and A. Zunger, Polymorphous band structure model of gapping in the antiferromagnetic and paramagnetic phases of the mott insulators MnO, FeO, CoO, and NiO, Phys. Rev. B **97**, 035107 (2018).
[49] X.-G. Zhao, Z. Wang, O. I. Malyi, and A. Zunger, Effect of static local distortions vs. dynamic motions on the stability and band gaps of cubic oxide and halide perovskites, Mater. Today **49**, 107 (2021).
[50] G. A. Sawatzky and J. W. Allen, Magnitude and Origin of the Band Gap in Nio, Phys. Rev. Lett. **53**, 2339 (1984).
[51] V. I. Anisimov, I. V Solovyev, M. A. Korotin, M. T. Czyżyk, and G. A. Sawatzky, Density-functional theory and NiO photoemission spectra, Phys. Rev. B **48**, 16929 (1993).
[52] J. Varignon, M. Bibes, and A. Zunger, Origins versus fingerprints of the Jahn-Teller effect in d-electron ABX_3 perovskites, Phys. Rev. Res. **1**, 033131 (2019).
[53] Z. Wang, O. I. Malyi, X. Zhao, and A. Zunger, Mass enhancement in 3d and s-p perovskites from symmetry breaking, Phys. Rev. B **103**, 165110 (2021).
[54] O. I. Malyi, X.-G. Zhao, A. Bussmann-Holder, and A. Zunger, Local positional and spin symmetry breaking as a source of magnetism and insulation in paramagnetic $EuTiO_3$, Phys. Rev. Mater. **6**, 034604 (2021).
[55] B. Alling, T. Marten, and I. Abrikosov, Questionable collapse of the bulk modulus in CrN, Nat. Mater. **9**, 283 (2010).
[56] X.-G. Zhao, G. M. Dalpian, Z. Wang, and A. Zunger, Polymorphous nature of cubic halide perovskites, Phys. Rev. B **101**, 155137 (2020).
[57] Z. Wang, X.-G. Zhao, R. Koch, S. J. L. Billinge, and A. Zunger, Understanding electronic peculiarities in tetragonal FeSe as local structural symmetry breaking, Phys. Rev. B **102**, 235121 (2020).
[58] W.-B. Zhang, Y.-L. Hu, K.-L. Han, and B.-Y. Tang, Pressure dependence of exchange interactions in NiO, Phys. Rev. B **74**, 054421 (2006).

[59] A. I. Liechtenstein, M. I. Katsnelson, V. P. Antropov, and V. A. Gubanov, Local spin density functional approach to the theory of exchange interactions in ferromagnetic metals and alloys, J. Magn. Magn. Mater. **67**, 65 (1987).

[60] V. P. Antropov, The exchange coupling and spin waves in metallic magnets: removal of the long-wave approximation, J. Magn. Magn. Mater. **262**, L192 (2003).

[61] A. Franceschetti, S. V Dudiy, S. V Barabash, A. Zunger, J. Xu, and M. van Schilfgaarde, First-Principles Combinatorial Design of Transition Temperatures in Multicomponent Systems: The Case of Mn in GaAs, Phys. Rev. Lett. **97**, 047202 (2006).

[62] B. Skubic, J. Hellsvik, L. Nordström, and O. Eriksson, A method for atomistic spin dynamics simulations: implementation and examples, J. Phys. Condens. Matter **20**, 315203 (2008).

[63] T. Archer, C. D. Pemmaraju, S. Sanvito, C. Franchini, J. He, A. Filippetti, P. Delugas, D. Puggioni, V. Fiorentini, R. Tiwari *et al.*, Exchange interactions and magnetic phases of transition metal oxides: benchmarking advanced ab initio methods, Phys. Rev. B **84**, 115114 (2011).

[64] G. Fischer, M. Däne, A. Ernst, P. Bruno, M. Lüders, Z. Szotek, W. Temmerman, and W. Hergert, Exchange coupling in transition metal monoxides: electronic structure calculations, Phys. Rev. B **80**, 014408 (2009).

[65] P. Gopal, R. De Gennaro, M. S. dos Santos Gusmao, R. Al Rahal Al Orabi, H. Wang, S. Curtarolo, M. Fornari, and M. Buongiorno Nardelli, Improved electronic structure and magnetic exchange interactions in transition metal oxides, J. Phys. Condens. Matter **29**, 444003 (2017).

[66] D. P. Landau and K. Binder, *A Guide to Monte Carlo Simulations in Statistical Physics*, 4th ed. (Cambridge University Press, Cambridge, 2014).